

Andreev bound states in a few-electron quantum dot coupled to superconductorsYulin Ma,¹ Tianqi Cai,¹ Xiyue Han,¹ Yaowen Hu,² Hongyi Zhang,¹ Haiyan Wang,¹ Luyan Sun,¹ Yipu Song,^{1,*} and Luming Duan^{1,†}¹*Center for Quantum Information, IIIS, Tsinghua University, Beijing 100084, China*²*Department of Physics, Tsinghua University, Beijing 100084, China*

(Received 19 September 2018; revised manuscript received 15 November 2018; published 8 January 2019)

A direct measurement of the density of Andreev bound states (ABSs) is experimentally investigated in a superconductor–quantum dot–superconductor hybrid nanowire system. A hard proximity-induced superconducting gap is observed, arising from superconducting correlations, in the transport spectrum of the hybrid system. Conductance peaks observed inside the superconducting gap reveal that the subgap states participate in the transport of the hybrid junction. We explore the evolution of low-energy Andreev bound states in a few-electron quantum dot (QD) coupled to superconductors, by probing the magnetic field dependence of exquisite detailed conductance spectra with a small bias voltage applied on the superconducting lead. In the presence of low magnetic fields, the resonance current is enhanced and broadened, attributed to the transport through Andreev bound states in QD, as the energy of ABSs reaches the threshold set by the applied bias voltage with the increase of the magnetic field. The simulated transport spectrum matches the experimentally observed evolution patterns of conductance, further implying the superconducting correlation nature of the observed electron transport. At high magnetic fields, the conductance maxes as the Fermi level reaches the degeneration point of Landau levels, leading to conductance peaks shown in the alternating narrow and wide patterns of Coulomb blockade oscillations.

DOI: [10.1103/PhysRevB.99.035413](https://doi.org/10.1103/PhysRevB.99.035413)**I. INTRODUCTION**

InAs nanowires continue to attract much attention as an interesting one-dimensional material for nanoscale circuits [1], single electron charge sensing [2], and potentially for spin-based [3] and topological quantum information processing [4]. Electron transport behavior in one-dimensional (1D) quantum wires is of fundamental and practical interest. Nanoscale electronic devices in contact with superconducting leads exhibit a large variety of fundamental physical phenomena. When two superconductors are coupled by a weak link, a dissipationless supercurrent can flow through the junction as a result of the proximity effect [5,6], which has a microscopic origin in Andreev reflection. The nature of the weak link can be of many different kinds including an insulator, a normal conductor, or a semiconducting nanowire. The semiconducting nanowire version of the weak link offers a possibility to tune the coupling strength with a gate voltage, and thus, allows for control of the magnitude of the supercurrent and implementation of a frequency tunable gmon superconducting qubit [7,8]. In addition, the unique properties of such hybrid nanodevices make them promising platforms to study fundamental phenomena such as quantum interference effects [9] and Majorana fermions [4,10–13]. The proximity effect has been recently demonstrated in one-dimensional semiconducting nanowires, where strong spin-orbit interactions can give

rise to Majorana bound states [4,10,11,13]. Among a variety of nanowires tested in experiments, InAs nanowires have high electron mobilities [14] and can easily form ohmic contacts [15]. The quasi-one-dimensional nature of electron transport at low temperatures [16] together with a strong spin-orbit coupling makes InAs nanowire an attractive material for the development of spintronic devices such as electron spin qubits in gate-defined quantum dots [3].

When a quantum dot is connected to superconducting electrodes, the proximity effect drastically modifies the electronic structure of the quantum dot and forms new subgap eigenstates, which are known as Andreev bound states (ABSs) [12,17–20]. ABSs carry a supercurrent in Josephson junctions, and thus, constitute a model system to investigate the superconducting proximity effect in QDs. The Josephson current in nanowires has been recently investigated at zero bias, and multiple Andreev reflections have been observed at a finite bias voltage [18–20]. It shows that quantum dots connected to superconducting electrodes can be tuned from a Coulomb blockade regime, to a Kondo regime, by changing local gate voltages [18–21]. When such hybrid structures are exposed to magnetic fields, the proximity effect allows for interplay between superconductivity and magnetism, giving rise to a variety of interesting effects. However, many aspects of the dependency of magnetic field have not been explored yet in superconductor–quantum dot–superconductor (S-QD-S) hybrid structures. In this paper, we report an experimental approach to measure a direct spectroscopy of the density of Andreev bound states in a S-QD-S hybrid nanowire system, and demonstrate the evolution of low-energy Andreev bound states, featuring an enhancement and

*ypsong@mail.tsinghua.edu.cn

†lmduan@tsinghua.edu.cn

broadening of resonance current in the presence of a magnetic field.

II. RESULTS AND DISCUSSION

A. Device Fabrication

The intrinsic donor-like surface states of InAs play a major role in determining transport properties [22], leading to reduced electron mobilities at low temperatures due to the ionized impurity scattering [14]. Fluctuations due to charge traps can vary in time due to carrier trapping and detrapping events, resulting in the random telegraph noise in the device conductance [23]. The presence of shell structures in InAs nanowires strongly reduces the random telegraph noise and smoothes out the distortions of local potential inside the core nanowire. InAlAs epitaxial shells could offer significant improvement to the quality of nanoelectronic devices, leading to a coherence transport in InAs nanowires [24]. Thus, we used core-shell InAlAs/InAs nanowires to fabricate S-QD-S junction devices. Core-shell nanowires were grown in a gas source molecular beam epitaxy system using Au seed particles. Transmission electron microscopy images of typical nanowires reveal that the nanowires have an inner core and an outer shell structure with low stacking fault densities. Both core and shell exhibit wurtzite single-crystal structure. In general, nanowires have a core diameter of 20~100 nm and a shell with 10~15 nm thickness, independent of the core diameter. The energy-dispersive x-ray spectroscopy line scan analysis along the radial direction shows In and As in the core region and In, As, and Al in the shell region with about 20% Al concentration ($\text{In}_{0.8}\text{Al}_{0.2}\text{As}$). The S-QD-S devices were fabricated using a standard e-beam lithography technique. As-grown nanowires were mechanically deposited onto a 300-nm-thick SiO_2 layer above a $n^{++}\text{-Si}$ substrate. Selected nanowires were located relative to prefabricated markers by scanning electron microscopy (SEM), with care taken to minimize the electron dose. The contact areas were etched with citric acid to remove the shell material, followed by room temperature sulfur passivation to prevent regrowth of the oxide layer during the transfer of the sample to an e-beam metal evaporator [15]. An Nb superconducting film (100 nm) was sputtered on the etched areas to yield ohmic contact. The device structure is shown schematically in Fig. 1(a), and the SEM image of a typical hybrid device is shown in Fig. 1(b). After fabrication, the device chip was wire-bonded and loaded onto the mix chamber of a dilution refrigerator. Transport measurements were carried out at a base temperature about 10 mK unless otherwise mentioned. RC, π , and copper powder filters in the measurement circuit were used to filter out measurement noise. Upon applying a DC source-drain voltage V_{sd} , the device current I_{sd} was measured using a current-voltage preamplifier at a noise floor of 0.5 pA/Hz. A voltage V_g applied to the degenerately doped Si substrate provided a global back gate.

B. Superconducting Correlations in the S-QD-S Hybrid Device

We investigated eight devices, with a source-drain channel length in a range between 300 to 570 nm, to varying levels of detail. We found that Coulomb blockade behaviors are present

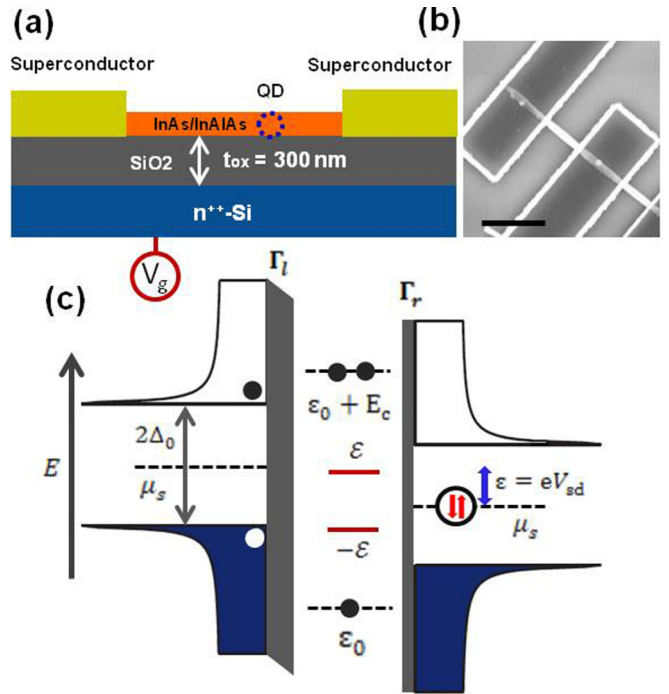


FIG. 1. (a) Schematic cross section of the S-QD-S hybrid nanowire device. (b) SEM image of a measured hybrid device. The scale bar is 500 nm. (c) Schematics of a S-QD-S device with tunnel couplings to the superconducting probe (Γ_l) and reservoir (Γ_r), respectively. Δ_0 is the superconducting energy gap, μ_s is the chemical potential of the superconducting lead, ϵ_0 is the orbital energy of the dot, E_c is the charging energy of the dot, $\pm\epsilon$ represents the energy levels of Andreev bound states in the subgap, V_{sd} is the bias voltage applied on the superconducting lead. In tunnel spectroscopy measurements, an electric current measured at $|V_{sd}| < \Delta_0/e$ is carried by Andreev bound states, transferring quasiparticles from the superconducting probe, to a Cooper pair in the superconducting reservoir. The alignment of μ_s to an energy level of ABSs yields a conductance peak.

in three devices. Figure 2(a) shows typical conductance curves versus the back gate for a device with a source-drain voltage $V_{sd} = 1.0$ mV, in the presence of a perpendicular magnetic field 0 and 5 T for the black and red curves, respectively. We have also measured Coulomb blockade peaks with different source-drain voltages at the magnetic field $B = 0$ T, as shown in Fig. S2 in the Supplemental Material [25]. The measured device has a nanowire with a core diameter of 89 nm, a shell diameter of 119 nm, and a channel length of 510 nm, with uncertainties ± 2 nm. The conductance of the hybrid device decreases with decreasing back gate voltages. At a zero magnetic field, the conductance emerges into a Coulomb blockade regime below $V_g = -2.95$ V, and is completely pinched off when $V_g < -3.2$ V. A series of resonance current peaks develops in the region of -3.20 V $< V_g < -2.95$ V. In the presence of a perpendicular magnetic field, the conductance is overall suppressed compared to the case at the zero magnetic field. The Coulomb blockade oscillations are well developed in the entire sweep range of the back gate voltage -3.20 V $< V_g < -2.80$ V. Differential conductance was measured for the device as a function of source-drain voltage V_{sd} , as shown

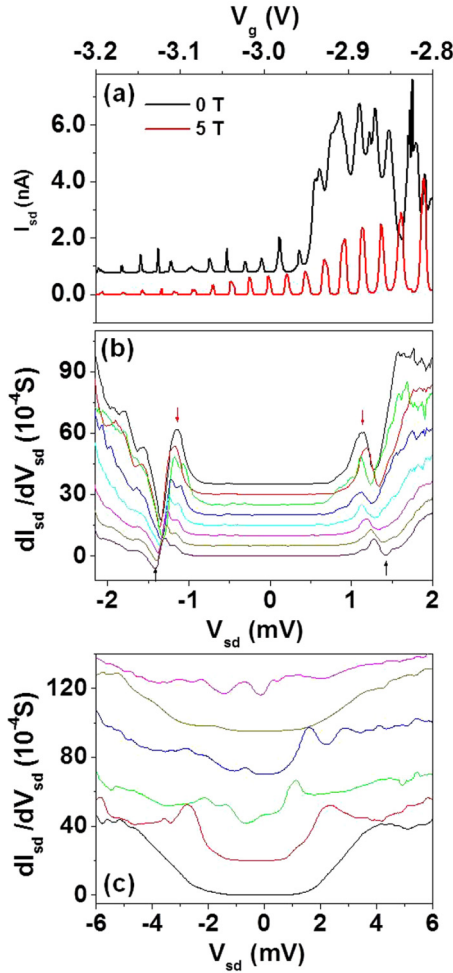


FIG. 2. (a) Typical conductance curves versus back gate for a device measured at 10 mK with a source-drain voltage $V_{sd} = 1.0$ mV, in the presence of a perpendicular magnetic field 0 and 5 T for the black and red line, respectively. The curve in black is shifted up 0.8 y-axis unit for clarity. (b) Differential conductance as a function of source-drain voltage V_{sd} with different back gate voltages V_g at a zero magnetic field. Eight conductance curves from bottom to top are measured at $V_g = -3.009, -3.008, -3.007, -3.006, -3.005, -3.004, -2.986$, and -2.985 V, respectively. For clarity, the conductance curves in dark yellow, magenta, cyan, blue, green, red, and black are shifted up 5, 10, 15, 20, 25, 30, and 35 y-axis units, respectively. Conductance peaks inside the superconducting gap, marked by red arrows, reveal that the subgap states participate in the transport of the S-QD-S hybrid junction. (c) Differential conductance as a function of source-drain voltage V_{sd} with different back gate voltages V_g at $B = 3.078$ T. Six conductance curves from bottom to top are measured at $V_g = -2.9994, -3.0046, -3.011, -3.0144, -3.0238$, and -3.0324 V, respectively. For clarity, the curves in red, green, blue, dark yellow, and magenta are shifted up 20, 40, 70, 95, and 115 y-axis units, respectively.

in Fig. 2(b), at zero magnetic field with different back gate voltages V_g . A hard proximity-induced superconducting gap, marked by two black arrows indicating the vanishing of the conductance, can be seen in the transport spectrum. The width of the gap in bias voltage is given by $2\Delta_0/e$, where Δ_0 is the effective superconducting gap. The value of Δ_0 is found

to be about 1.3 meV, which is consistent with the reported value for evaporated thin Nb films [26,27]. Each conductance curve features two peaks, illustrated by red arrows, positioned nearly symmetrically with respect to the zero-bias point in the superconducting gap. Peak positions vary slightly with changes in back gate voltages. For instance, the peak shifts consistently from -1.14 to -1.27 mV by sweeping the back gate voltage from -2.985 to -3.009 V. These conductance peaks inside the superconducting gap unambiguously reveal that the subgap states participate in the transport of S-QD-S hybrid junction. However, when a perpendicular magnetic field of 3.078 T is applied, the measured conductance gap has a strong dependency on gate voltages, as shown in Fig. 2(c), referring to a gate-voltage modulation of typical Coulomb blockade patterns. No subgap resonance patterns are observed for the conductance curves. This reveals the vanishing of the superconductivity in Nb contact leads at such a strong magnetic field.

To clarify these superconducting correlation features in the conductance spectrum, we measured differential conductance for the device as a function of bias voltage V_{sd} and back gate voltage V_g . Figures 3(a) and 3(b) show the differential conductance for the measured device with varying the back gate voltage V_g and bias voltage V_{sd} at a magnetic field $B = 0$ T and $B = 3.078$ T, respectively. In the presence of the high magnetic field, we have observed regular Coulomb oscillation patterns. The charging energy extracted from the measurement is about $E_c \sim 3.1$ meV, corresponding to a dot capacitance, $c \sim 51.6$ aF. The addition energy is around 21.9 meV. Thus, the lever arm is estimated to be 14.2% for conversion of gate voltages into energies. The gate capacitance per unit length c_g can be estimated as the capacitance of a wire above an infinite conducting plane (c'_g) in series with the cylindrical capacitance between the core and shell (c'_s), i.e., $\frac{1}{c_g} = \frac{1}{c'_g} + \frac{1}{c'_s}$. $c'_s = \frac{2\pi\epsilon_0\epsilon_r(\text{shell})}{\ln(\frac{R_s}{R_c})}$, where R_s, R_c is the radius of nanowire shell and core, respectively, and $\epsilon_r(\text{shell})$ is taken as 12.46 for the dielectric constant of the $\text{In}_{0.8}\text{Al}_{0.2}\text{As}$ shell [28]. The parameter $c'_g = 2\pi\epsilon_0\epsilon_r/\cosh^{-1}(\frac{R_s+t_{ox}}{R_s})$, where ϵ_r is the SiO_2 dielectric constant and t_{ox} the thickness of SiO_2 layer [29,30]. The equation above assumes that the nanowire is embedded in SiO_2 . To compensate for the fact that the nanowire actually sits atop the SiO_2 and is surrounded by the vacuum, it was shown by Wunnicke that a modified dielectric constant $\epsilon_r = 2.2$ can be taken [29]. The calculated gate capacitance per unit length c_g is 48.3 pF/m for a nanowire with $2R_c = 89$ nm and $2R_s = 119$ nm sitting on an oxide layer of 300 nm. The lever arm can be estimated by the ratio of gate capacitance to total capacitance of QD, i.e., $c_g \cdot d/c$, where d is an effective gating length associated with the QD size. The distance between the two confinement barriers along the nanowire axis may be larger than the QD size. Furthermore, except for the electric field underneath the QD, the fields distributed nearby the QD location also contribute the electrical gating effect for the QD. Thus, the effective gating length should be larger than the QD size. To do a rough order-of-magnitude estimation, we used a parameter $d = 119$ nm, which is the shell diameter of the nanowire, to estimate the lever arm to be about 11.1%. Based on a simple model of a spherical QD, the size of quantum dot can be estimated to be $R = \frac{c}{4\pi\epsilon_0\epsilon_r(\text{core})} \sim 31$ nm, where R is

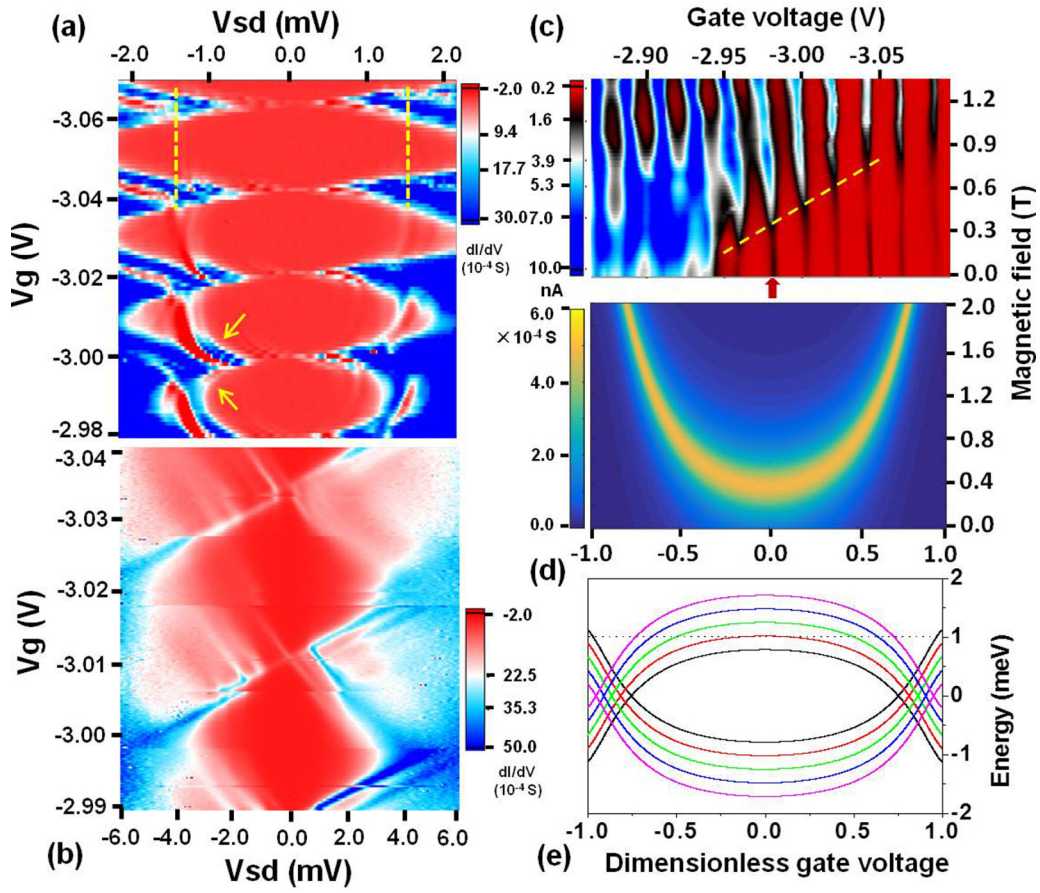


FIG. 3. Differential conductance of the measured device as a function of the back gate voltage V_g and bias voltage V_{sd} with a perpendicular external magnetic field $B = 0$ T (a) and $B = 3.078$ T (b), respectively. Coulomb diamond patterns in (b) are significantly modulated at a zero magnetic field. Resonance patterns of Andreev bound states, marked by yellow arrows, emerge inside the superconducting gap arising from superconducting correlations. (c) The spectrum of transport current as a function of the back gate voltage and magnetic field with $V_{sd} = 1.0$ mV. The resonance current peak is enhanced and broadened at a particular magnetic field. The overall trend of the transition value of magnetic field increases as sweeping the back gate voltage to more negative. (d) A simulation of conductance resonant patterns corresponding to the odd occupation valley at $V_g = -2.982$ V in (c). The simulated conductance peak is broadened as the magnetic field goes up to 0.38 T. The dimensionless gate voltage $x = 1 + \frac{2\varepsilon_0}{E_c}$. $x = 0$ marks the center of the odd valley. The parameters used for the calculation are taken as $E_c = 3.1$ meV, $\Delta_0 = 1.3$ meV, $V_{sd} = 1.0$ mV, $\phi = \pi/3$, $\frac{\Gamma_\alpha}{E_c} = 0.135$, $g_{ce} = 0$, $g_d = 10$. (e) Energy levels of Andreev bound states (the energy difference between $|D\rangle$ and $|S\rangle$) at different magnetic fields $B = 0, 0.4, 0.8, 1.2$, and 1.6 T for the black, red, green, blue, and magenta curve, respectively. The parameters used for simulation are $E_c = 3.1$ meV, $\Delta_0 = 1.3$ meV, $V_{sd} = 1.0$ mV, $\phi = \pi/3$, $\frac{\Gamma_\alpha}{E_c} = 0.135$, $g_{ce} = 0$, $g_d = 10$. The black dashed line at 1.0 meV marks the bias window in the measurement.

the radius of the dot, and $\varepsilon_{r(\text{core})}$ is 15.15 for the dielectric constant of the InAs core [31]. Given the channel length $L = 510$ nm, this estimated value indicates that the quantum dot is small compared to the channel length, revealing an unintentional quantum dot forming inside the nanowire channel. We attribute this QD confinement to the spatial electrostatic potential fluctuations along the nanowire. It is known that charged surface states produce a random spatial electrostatic potential along the nanowire, which may contribute to the spontaneous formation of quantum dots at low temperature [32]. These fluctuations may be due to surface defects [33], stacking faults [32], or charge traps in the native oxide layer of nanowire [23].

At zero magnetic field, the Coulomb diamond patterns are significantly modulated. Compared to the well-defined Coulomb diamond patterns shown in Fig. 3(b), clear resonance current patterns, indicated by yellow arrows in Fig. 3(a),

emerge inside the superconducting gap arising from superconducting correlations. The superconducting gap is marked by two yellow dashed lines in the figure. The subgap resonance pattern has a dependency on gate voltages, which is consistent with the gate-voltage dependence of subgap conductance peaks shown in Fig. 2(b). We attribute subgap resonance patterns to Andreev bound states associated with the quantum dot, induced by superconducting correlations of the Nb leads with its proximity to the nanowire channel. Our device can be implemented as the elements of two superconducting leads (S) with an energy gap Δ_0 , each tunnel coupled to a QD with a coupling strength Γ_α via a normal semiconductor section (N), in a configuration of S-N-QD-N-S, where $\alpha = l, r$ labels the left and right contacts. The InAs nanowires used in devices have a typical elastic mean free path of $l_e \sim 50$ nm [20], significantly shorter than the junction length, indicating that the transport is in the diffusive regime in the device.

We can characterize the diffusive transport in such a device with a Thouless energy, $E_{\text{th}} = \frac{\hbar D}{L^2} \sim 0.042$ meV, where D is the diffusion coefficient, $D = l_e V_e/3 \sim 166 \text{ cm}^2 \cdot \text{s}^{-1}$, $V_e \sim 10^6$ m/s is the Fermi velocity of electrons in InAs [20,34], L is the channel length. Considering the measurement temperature 10 mK and electron temperature of measurement circuits around 80 mK, we estimated the thermal length to be $l_T = (\hbar D/k_B T)^{1/2} \sim 1.26 \text{ } \mu\text{m}$, where T is the temperature and k_B is the Boltzmann constant. At such a low measurement temperature, the phase coherence length of InAs nanowire can be on the order of $l_\phi \sim 500$ nm [16,34]. Within the context of this model, the presence of normal sections results in a rescaling of the S-QD coupling strength Γ_α . For our measured device, the normal semiconductor section between the QD and superconducting lead is assumed to be shorter than the thermal length but close to the phase coherence length. The normal sections can transfer superconducting correlations to the QD through the Andreev reflection process. However, since the proximity effect originates from the phase coherent Andreev reflections at S-N interfaces, the energy scales of the coherent states in the normal region would decay as the length of the normal section increases. This may be the reason why subgap resonance patterns in Fig. 3(a) are relatively weak, as discussed further below. We have also measured the differential conductance of the device as varying the back gate voltage V_g and bias voltage V_{sd} over a different sweep range at the magnetic field $B = 0$ T, as shown in Fig. S1 in the Supplemental Material [35]. The reproducible resonance patterns presented in Figs. 3(a) and S1 reveal that the quantum dot is stable although it is formed unintentionally inside the nanowire channel.

An effective Hamiltonian can be used to implement a quantum dot coupled to two superconducting leads $H_{\text{eff}} = H_{\text{QD}} + H_S + H_T$ [17,18,20]. Here H_{QD} , H_S , and H_T represent the Hamiltonian for the uncoupled quantum dot, two superconducting leads, and the coupling between the leads and QD, respectively. The Hamiltonian of the QD is given by $H_{\text{QD}} = \sum_{\sigma=\uparrow,\downarrow} \varepsilon_0 d_\sigma^\dagger d_\sigma + E_c n_\uparrow n_\downarrow$, where ε_0 is the orbital energy of the dot, E_c is the charging energy, d_σ is the annihilation operator of an electron in the dot with spin state σ . The coupling Hamiltonian is $H_T = \sum_{\alpha\sigma} (t_\alpha c_{\alpha\sigma}^\dagger d_\sigma + t_\alpha^* d_\sigma^\dagger c_{\alpha\sigma})$, where t_α denotes the lead-dot tunneling amplitudes and the lead index α refers to the two superconducting leads. When the charging energy is small compared to the superconducting gap, $E_c < \Delta_0$, in the absence of an external magnetic field the eigenstates of H_{eff} are two degenerate spin 1/2 doublet states $|\uparrow\rangle$, $|\downarrow\rangle$ and two singlet states $|+\rangle$, $|-\rangle$ which are superpositions of the doubly occupied $|\uparrow\downarrow\rangle$ and empty $|0\rangle$ states of the quantum dot [18,20]. In our case, the charging energy $E_c > \Delta_0$, instead of forming a singlet state with the empty and doubly occupied states, the unpaired spin in the quantum dot forms a Yu-Shiba-Rusinov singlet with quasiparticles in the superconducting leads [17,19,20,36], because it has a much lower required energy compared to the previous case. When the QD is tuned in an even valley, the ground state is always singlet. However, in an odd valley, the system has two possible ground states, a doublet $|D\rangle$ or a singlet $|S\rangle$, determined by the competition between the local energy E_c , Δ_0 , and Γ_α . A small ratio of Γ_α/E_c leads to a singlet excitation state and a doublet ground state [19,36]. In Fig. 3(a), 11 electrons, counting

from the zero electron regime determined by the pinch-off threshold voltage, occupy the quantum dot in an odd valley with $-2.998 \text{ V} < V_g < -2.980 \text{ V}$. The Yu-Shiba-Rusinov states hosted in this odd valley have a strong dependency on the gate voltage. The energy of singlet $|S\rangle$ trends to lower as the gate voltage is swept towards the odd-even transition at $V_g = -2.998 \text{ V}$, as indicated by the yellow arrow in Fig. 3(a). We calculated the energy of the Andreev bound states using a method [17,37] discussed in more detail in the Supplemental Material [38]. The simulation result, as shown in Fig. 3(e), reveals that the energy of Andreev bound states (the energy difference between $|D\rangle$ and $|S\rangle$) has a dependency on the gate voltage, trending to lower and taking a singlet-doublet switch at the odd-even valley transition [10,18]. The parameter x is a dimensionless gate voltage defined as $x = 1 + \frac{2\varepsilon_0}{E_c}$, and $x = 0$ marks the center of the odd valley. The parameters used for the calculation are taken as $E_c = 3.1$ meV, $\Delta_0 = 1.3$ meV, $V_{\text{sd}} = 1.0$ mV, $\phi = \pi/3$, $\frac{\Gamma_\alpha}{E_c} = 0.135$, $g_{\text{ce}} = 0$, $g_d = 10$ [20], where ϕ is the phase difference between superconducting leads.

C. Evolution of Low-energy Andreev Bound States at Low Magnetic Fields

When such a hybrid structure is exposed to a magnetic field, the proximity effect allows for interplay between superconductivity and magnetism. Magnetoconductance signatures of sub-band structures have been experimentally investigated in InAs nanowires with normal metal source-drain contacts and an axial magnetic field [39]. Instead of focusing on the InAs nanowire, we explored the evolution of low-energy Andreev bound states in a single quantum dot coupled to superconductors, by probing the conductance as a function of a back gate voltage and a magnetic field perpendicular to the substrate. We used Nb as the superconducting leads, which allow us to apply the magnetic field higher than that in previously referenced studies [20] without destroying the superconductivity. Therefore, we can observe the evolution of the low-energy Andreev bound states into Landau states upon the increase of the magnetic field. In Fig. 3(c), we show resonance current patterns in the S-QD-S device as varying the back gate voltage and magnetic field from 0 to 1.35 T, below the critical magnetic field of Nb leads [40]. Instead of sweeping the bias voltage and gate voltage at only certain magnetic fields [10], we fixed a small bias voltage of 1.0 mV applied to the device to consistently probe the magnetic field dependence of the exquisite detailed energy-level spectra in the superconductor contacted InAs QD. In such a measurement, an electric current measured at $|V_{\text{sd}}| < \Delta_0/e$ is carried by the Andreev bound states, transferring quasiparticles from the superconducting probe, to a Cooper pair in the superconducting reservoir, as depicted in Fig. 1(c) in the schematics of a QD with tunnel couplings to the superconducting probe and reservoir. A quasiparticle tunneling from the edge of the filled negative energy states of the left superconductor can become an electron in the normal section. The electron entering the QD from the normal section induces a single-electron transition from the ABS ground state doublet $|D\rangle$, to the first excited state singlet $|S\rangle$. The excited state relaxes back to the ground state and an Andreev reflection at the superconductor–

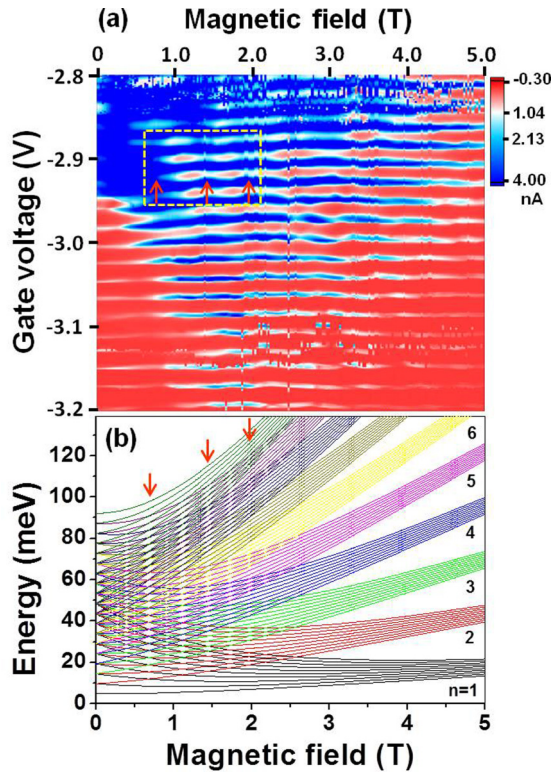


FIG. 4. (a) Energy spectroscopy of the S-QD-S hybrid system in a high magnetic field up to 5 T in a range of back gate voltage $-3.2 \text{ V} < V_g < -2.8 \text{ V}$ with $V_{sd} = 1.0 \text{ mV}$. (b) The simulated magnetic field dependence of the energy spectrum of Landau levels for n from one to ten with $l = 1 \sim 10$. A parabolic confinement of 4.85 meV is used for calculation.

QD interface generates a Cooper pair in the superconducting reservoir and reflects a hole. The process yields a resonance current when an Andreev level at $\varepsilon = eV_{sd}$, where ε is the energy difference between $|D\rangle$ and $|S\rangle$ [19,36]. The energies of Andreev bound states, $\pm\varepsilon$, can be tuned by the dot chemical potential μ through the applied back gate voltage V_g . When a magnetic field is applied, the energy of singlet states remains. However, the two doublets, $|\uparrow\rangle$ and $|\downarrow\rangle$, gain Zeeman energies of $\pm\frac{1}{2}g_d\mu_B B$ respectively, where g_d is the Landé g factor in the quantum dot and μ_B is the Bohr magneton. Only the transition from the ground doublet state $|\uparrow\rangle$ to the excited singlet state is allowed. Unique resonance current patterns emerge corresponding to the transport through the Andreev bound states in the QD, as shown in Fig. 3(c). The spin parity alternates for the adjacent resonance patterns of current by switching the even or odd occupation of electrons in the QD. The resonance current peak at $V_g = -2.982 \text{ V}$, marked by a red arrow in the figure, attributes to a transition from the excited state $|S\rangle$ to the ground state $|D\rangle$, where 11 electrons are estimated to occupy the quantum dot. As the magnetic field increases from zero, the resonance current peak is enhanced and broadened at a particular magnetic field. Moreover, except for the first three Coulomb oscillation peaks in a range of $-3.2 \text{ V} < V_g < -3.15 \text{ V}$ [see Fig. 4(a)], the overall trend of the transition value of the magnetic field increases as the back gate voltage is swept to the more negative side, as indicated

by a yellow dashed line in the figure. For instance, the current resonance peak at $V_g = -2.958, -2.982, -3.004 \text{ V}$ is enhanced and broadened as the magnetic field reaches the transition value of 0.2414, 0.3234, and 0.5344 T, respectively. These unique features of enhancement and broadening of resonance currents in the presence of a magnetic field have not been observed previously. The observation cannot be explained by the magnetic field dependence of quantized energy levels in a quantum dot. It should be related to the superconducting correlations of electron transport in the S-QD-S hybrid junction. The resonance current is enhanced and restored to the regular Coulomb oscillation patterns as the magnetic field is above the transition value, revealing that the energy of the Andreev bound state involved in the transport goes beyond the superconducting gap. To elucidate the evolution of resonance current patterns, we calculated the magnetic field dependence of the energy-level spectrum of Andreev bound states in the QD (see the simulation method in the Supplemental Material for details [38]). Figure 3(e) shows energy levels of Andreev bound states at different magnetic fields $B = 0, 0.4, 0.8, 1.2$, and 1.6 T , respectively. The simulation of energy spectrum is corresponding to the odd valley at $V_g = -2.982 \text{ V}$, labeled by a red arrow in Fig. 3(c). A dashed line at 1.0 meV in the figure marks the bias window in the measurement. It can be seen that the energy of Andreev bound states goes up as the magnetic field increases, which is consistent with previous studies [10]. The applied bias voltage of 1.0 mV sets a threshold for the maximum point of the energy spectrum to approach. Once the energy of Andreev bound states reaches the threshold, intersections of the energy spectrum and the threshold falls apart as the Andreev bound state energy goes up further, resulting in an enhancement and broadening of the current resonant peak. At low temperatures and small applied voltages (small compared to the spacing of the bound states ΔE), conduction through the quantum dot occurs via resonant tunneling through a single Andreev bound state. We used the Breit-Wigner formula [41,42] to calculate the conductance through the S-QD-S hybrid junction, i.e., $G = \frac{2e^2}{h} \frac{\Gamma_l \Gamma_r}{\varepsilon_R^2 + \frac{1}{4}\Gamma^2}$, where ε_R is the energy of ABSs, relative to the chemical potential μ_s in the reservoirs; Γ_l, Γ_r are the tunnel coupling of the QD to the superconducting probe and reservoir, respectively. We denote $\Gamma = \Gamma_l + \Gamma_r$. This formula holds under the condition $\Gamma \ll k_B T \ll \Delta E$. A simulation of conductance resonant patterns is shown in Fig. 3(d). The parameters used for the simulation are taken as $E_c = 3.1 \text{ meV}$, $\Delta_0 = 1.3 \text{ meV}$, $V_{sd} = 1.0 \text{ mV}$, $\phi = \pi/3$, $\frac{\Gamma_r}{E_c} = 0.135$, $g_{ce} = 0$, $g_d = 10$ [20]. The resonant pattern is enhanced and broadened as the magnetic field goes up to about 0.38 T. The more negative back gate voltage lowers the energy of Andreev bound states, and thus, it requires a higher magnetic field to reach the threshold to broaden the resonance current. The overall trend of the simulated low-magnetic field dependence is consistent with experimental observations, further implying the superconducting correlation nature of the observed electron transport. It is worth noting that we used a fixed phase difference for the simulation. In fact, the magnetic field slightly affects the superconducting phase difference, and thus, changes the energy level of ABS states. Taking into account the effect of phase difference [43], we

calculated the energy of Andreev bound states and simulated the conductance resonant patterns. The results are presented in Figs. S3 and S4 in the Supplemental Material [44].

D. Energy Spectroscopy at Higher Magnetic Fields

To investigate the energy spectroscopy of the hybrid system in a higher magnetic field, we swept the magnetic field up to 5 T with the back gate voltage $-3.2 \text{ V} < V_g < -2.8 \text{ V}$ and $V_{sd} = 1.0 \text{ mV}$, as shown in Fig. 4(a). The current is completely pinched off when $V_g < -3.2 \text{ V}$, where the threshold voltage V_{th} is defined. By weeping the gate voltage from -3.2 V to -2.8 V , the electron tunnels into QD one by one. Counting up from zero, 18 electrons occupy the quantum dot at $V_g = -2.8 \text{ V}$. The conductance is overall suppressed as the magnetic field is swept to the high-field region. As the energy of Andreev bound states goes beyond the superconducting gap by increasing the magnetic field, the Coulomb blockade oscillations dominate the transport. Coulomb blockade oscillations are modulated by the magnetic field, presenting alternating narrow and wide patterns with increasing the magnetic field. The most prominent alternating patterns are highlighted in a rectangle with yellow dashed lines in Fig. 4(a). Furrows of alternating patterns located at $B \sim 0.66, 1.42$, and 1.92 T , marked by red arrows, are corresponding to conductance peaks with changes of the magnetic field. To analyze this measurement observation, we calculated the magnetic field dependence of energy spectrum in a higher magnetic field up to 5 T. For a quantum dot defined by a two-dimensional parabolic confinement $\hbar\omega_0$, the energy spectrum of noninteracting electrons in a magnetic field is given by $E_{n,l} = \frac{1}{2}(n-l)\hbar\omega_c + \frac{1}{2}(n+l-1)\hbar\sqrt{\omega_c^2 + 4\omega_0^2}$, $n, l = 1, 2, 3 \dots$ [45], where $\omega_c = eB/m^*$ is the cyclotron frequency in a magnetic field B and $m^* = 0.023m_0$ is the electron effective mass in InAs [31]. Each state has twofold spin degeneracy, which is gradually lifted as the magnetic field is increased. Neglecting the spin splitting, we plotted the energy-level spectrum in Fig. 4(b), for n from one to ten with $l = 1 \sim 10$. The magnetic length, $l_B = \sqrt{\frac{\hbar}{eB}}$, is estimated to be smaller than the dot size when $B > 0.195 \text{ T}$, thus we expect the density of states to converge towards the Landau levels at a large magnetic field. The calculated energy spectrum indeed reveals some characteristics of low-energy Landau levels. The parabolic confinement $\hbar\omega_0$ is the only fitting parameter used for the simulation. We find that a value of $\hbar\omega_0 = 4.85 \text{ meV}$ yields a serial of degenerations of energy levels positioned at $B \sim 0.67, 1.43$, and 1.95 T , which best matches the

experimental observation of conductance peaks located at $B \sim 0.66, 1.42$, and 1.92 T . The dot size can be estimated to be $R \sim 29 \text{ nm}$ (radius) based on the parabolic confinement parameter [46], which is close to the value estimated from the dot capacitance. These degenerations of energy levels yield a maximum density of the energy spectrum. Thus, the conductance maximizes as the Fermi level reaches the degeneration point of Landau levels, leading to conductance peaks shown in the alternating narrow and wide patterns of Coulomb blockade oscillations.

III. CONCLUSIONS

In summary, we have investigated the evolution of low-energy Andreev bound states in a few-electron quantum dot coupled to superconductors, by probing the conductance as a function of the back gate voltage and magnetic field. We have observed a hard proximity-induced superconducting gap, arising from the superconducting correlation features, in the transport spectrum of the hybrid system. Conductance peaks observed inside the superconducting gap reveal that the sub-gap states participate in the transport of the hybrid junction. In the presence of a high magnetic field, the conductance maximizes as the Fermi level reaches the degeneration point of Landau levels, leading to conductance peaks shown in the alternating narrow and wide patterns of Coulomb blockade oscillations. At a low magnetic field, the resonance current is enhanced and broadened, attributed to the transport through Andreev bound states in QD, as the energy of ABSs reaches the threshold set by the applied bias voltage with the increase of the magnetic field. The simulated transport spectrum matches the experimentally observed evolution patterns of conductance, further implying the superconducting correlation nature of the observed electron transport. More positive back gate voltage could manifest the superconductor-QD-superconductor hybrid nanowire system in a topologically nontrivial regime. Potential application would be highly desirable, including the search for Majorana fermions and topological superconductivity in such a hybrid system.

ACKNOWLEDGMENTS

We thank Chengyao Li for technical support. We thank Jonathan Baugh at University of Waterloo and Ray R. LaPierre at McMaster University for nanowire growth. This work was supported by the National Natural Science Foundation of China under Grant No.11874235 and the State's Key Project of Research and Development Plan under Grant No. 2016YFA0301902.

The authors declare no competing financial interests.

- [1] S. W. Nam, X. C. Jiang, Q. H. Xiong, D. Ham, and C. M. Lieber, *Proc. Natl. Acad. Sci. USA* **106**, 21035 (2009).
- [2] J. Salfi, I. G. Savelyev, M. Blumin, S. V. Nair, and H. E. Ruda, *Nat. Nanotechnol.* **5**, 885 (2010).
- [3] S. Nadj-Perge, S. M. Frolov, E. P. A. M. Bakkers, and L. P. Kouwenhoven, *Nature (London)* **468**, 1084 (2010).

- [4] V. Mourik, K. Zuo, S. M. Frolov, S. R. Plissard, E. P. A. M. Bakkers, and L. P. Kouwenhoven, *Science* **336**, 1003 (2012).
- [5] S. Abay, H. Nilsson, F. Wu, H. Q. Xu, C. M. Wilson, and P. Delsing, *Nano Lett.* **12**, 5622 (2012).
- [6] H. A. Nilsson, P. Samuelsson, P. Caroff, and H. Q. Xu, *Nano Lett.* **12**, 228 (2012).

- [7] T. W. Larsen, K. D. Petersson, F. Kuemmeth, T. S. Jespersen, P. Krogstrup, J. Nygård, and C. M. Marcus, *Phys. Rev. Lett.* **115**, 127001 (2015).
- [8] G. de Lange, B. van Heck, A. Bruno, D. J. van Woerkom, A. Geresdi, S. R. Plissard, E. P. A. M. Bakkers, A. R. Akhmerov, and L. DiCarlo, *Phys. Rev. Lett.* **115**, 127002 (2015).
- [9] J. Kong, E. Yenilmez, T. W. Tombler, W. Kim, H. J. Dai, R. B. Laughlin, L. Liu, C. S. Jayanthi, and S. Y. Wu, *Phys. Rev. Lett.* **87**, 106801 (2001).
- [10] M. T. Deng, S. Vaitiekėnas, E. B. Hansen, J. Danon, M. Leijnse, K. Flensberg, J. Nygård, P. Krogstrup, and C. M. Marcus, *Science* **354**, 1557 (2016).
- [11] M. T. Deng, C. L. Yu, G. Y. Huang, M. Larsson, P. Caroff, and H. Q. Xu, *Nano Lett.* **12**, 6414 (2012).
- [12] C.-X. Liu, J. D. Sau, T. D. Stanescu, and S. Das Sarma, *Phys. Rev. B* **96**, 075161 (2017).
- [13] S. M. Albrecht, A. P. Higginbotham, M. Madsen, F. Kuemmeth, T. S. Jespersen, J. Nygård, P. Krogstrup, and C. M. Marcus, *Nature (London)* **531**, 206 (2016).
- [14] N. Gupta, Y. P. Song, G. W. Holloway, U. Sinha, C. M. Haapamaki, R. R. LaPierre, and J. Baugh, *Nanotechnology* **24**, 225202 (2013).
- [15] D. B. Suyatin, C. Thelander, M. T. Bjork, I. Maximov, and L. Samuelson, *Nanotechnology* **18**, 105307 (2007).
- [16] C. Blomers, M. I. Lepsa, M. Luysberg, D. Grutzmacher, H. Luth, and T. Schapers, *Nano Lett.* **11**, 3550 (2011).
- [17] G. Kiršanskas, M. Goldstein, K. Flensberg, L. I. Glazman, and J. Paaske, *Phys. Rev. B* **92**, 235422 (2015).
- [18] J. D. Pillet, P. Joyez, R. Zitko, and M. F. Goffman, *Phys. Rev. B* **88**, 045101 (2013).
- [19] Z. Su, Andreev bound states in superconductor-quantum dot chains, Ph.D. thesis, University of Pittsburgh, 2017.
- [20] W. Chang, Superconducting Proximity Effect in InAs Nanowires, Ph.D. thesis, Harvard University, 2014.
- [21] K. Gharavi, G. W. Holloway, R. R. LaPierre, and J. Baugh, *Nanotechnology* **28**, 085202 (2017).
- [22] S. A. Dayeh, *Semicond. Sci. Technol.* **25**, 024004 (2010).
- [23] G. W. Holloway, Y. P. Song, C. M. Haapamaki, R. R. LaPierre, and J. Baugh, *J. Appl. Phys.* **113**, 024511 (2013).
- [24] G. W. Holloway, Y. P. Song, C. M. Haapamaki, R. R. LaPierre, and J. Baugh, *Appl. Phys. Lett.* **102**, 043115 (2013).
- [25] See Supplemental Material at <http://link.aps.org/supplemental/10.1103/PhysRevB.99.035413> for Coulomb blockade peaks with different source-drain voltages at the magnetic field $B = 0$ T.
- [26] S. Bose, P. Raychaudhuri, R. Banerjee, P. Vasa, and P. Ayyub, *Phys. Rev. Lett.* **95**, 147003 (2005).
- [27] A. I. Gubin, K. S. Il'in, S. A. Vitusevich, M. Siegel, and N. Klein, *Phys. Rev. B* **72**, 064503 (2005).
- [28] M. Littlejohn, K. W. Kim, and H. Tian, in *Properties of Lattice-Matched and Strained Indium Gallium Arsenide*, edited by P. Bhattacharya (INSPEC, London, 1993), Sec. 4.2, pp. 107–116.
- [29] O. Wunnicke, *Appl. Phys. Lett.* **89**, 083102 (2006).
- [30] J. W. W. V. Tilburg, R. E. Algra, W. G. G. Immink, M. Verheijen, E. P. A. M. Bakkers, and L. P. Kouwenhoven, *Semicond. Sci. Technol.* **25**, 024011 (2010).
- [31] H. J. Joyce, C. J. Docherty, Q. Gao, H. H. Tan, C. Jagadish, J. Lloyd-Hughes, L. M. Herz, and M. B. Johnston, *Nanotechnology* **24**, 214006 (2013).
- [32] M. D. Schroer and J. R. Petta, *Nano Lett.* **10**, 1618 (2010).
- [33] S. A. Dayeh, C. Soci, P. K. L. Yu, E. T. Yu, and D. Wang, *J. Vac. Sci. Technol. B* **25**, 1432 (2007).
- [34] S. Abay, D. Persson, H. Nilsson, F. Wu, H. Q. Xu, M. Fogelström, V. Shumeiko, and P. Delsing, *Phys. Rev. B* **89**, 214508 (2014).
- [35] See Supplemental Material at <http://link.aps.org/supplemental/10.1103/PhysRevB.99.035413> for the differential conductance of the device as varying the bias voltage V_{sd} over a different sweep range at the magnetic field $B = 0$ T.
- [36] E. J. H. Lee, X. C. Jiang, M. Houzet, R. Aguado, C. M. Lieber, and S. De Franceschi, *Nat. Nanotechnol.* **9**, 79 (2014).
- [37] J. R. Schrieffer and P. A. Wolff, *Phys. Rev.* **149**, 491 (1966).
- [38] See Supplemental Material at <http://link.aps.org/supplemental/10.1103/PhysRevB.99.035413> for the simulation method.
- [39] G. W. Holloway, D. Shiri, C. M. Haapamaki, K. Willick, G. Watson, R. R. LaPierre, and J. Baugh, *Phys. Rev. B* **91**, 045422 (2015).
- [40] E. Andreas, S. Alexey, H. Heinz-Wilhelm, and S. Michael, *New Frontiers in Superconductivity Research*, edited by B. P. Martins (Nova Science Publishers Inc., New York, 2006), pp. 153–189.
- [41] C. W. J. Beenakker and H. van Houten, in *Single-Electron Tunneling and Mesoscopic Devices*, edited by H. Koch and H. Lübbig, Vol. 31 (Springer, Berlin, 1992), pp. 175–179.
- [42] C. W. J. Beenakker, *Phys. Rev. B* **44**, 1646 (1991).
- [43] A. Barone and G. Paternò, *Physics and Applications of the Josephson Effect* (Wiley, New York 2005), pp. 9–18.
- [44] See Supplemental Material at <http://link.aps.org/supplemental/10.1103/PhysRevB.99.035413> for calculating the energy of Andreev bound states and simulating the conductance resonant patterns.
- [45] T. Sakamoto, S. W. Hwang, Y. Nakamura, and K. Nakamura, *Appl. Phys. Lett.* **65**, 875 (1994).
- [46] S. Dey and Y. S. Jain, [arXiv:1002.4308v1](https://arxiv.org/abs/1002.4308v1).